Wei Huang
State Key Laboratory of Mechanics and
Control of Mechanical Structures,
Nanjing University of
Aeronautics and Astronautics,
Yudao Street 29,
Nanjing 210016, China
e-mail: huangwei91@nuaa.edu.cn

Hongli Ji
State Key Laboratory of Mechanics and
Control of Mechanical Structures,
Nanjing University of
Aeronautics and Astronautics,
Yudao Street 29,
Nanjing 210016, China;
Department of Mechanical Engineering,
Hong Kong Polytechnic University,
Hung Hom,
Kowloon 999077, Hong Kong
e-mail: jihongli@nuaa.edu.cn

Jinhao Qiu[1]
Fellow ASME
State Key Laboratory of Mechanics and
Control of Mechanical Structures,
Nanjing University of
Aeronautics and Astronautics,
Yudao Street 29,
Nanjing 210016, China
e-mail: qiu@nuaa.edu.cn

Li Cheng
Department of Mechanical Engineering,
Hong Kong Polytechnic University,
Hung Hom,
Kowloon 999077, Hong Kong
e-mail: li.cheng@polyu.edu.hk

Wave Energy Focalization in a Plate With Imperfect Two-Dimensional Acoustic Black Hole Indentation

The acoustic black hole (ABH) phenomenon in thin-walled structures with a tailored power-law-profiled thickness allows for a gradual change of the phase velocity of flexural waves and energy focalization. However, ideal ABH structures are difficult to realize and suffer from potential structural problems for practical applications. It is therefore important to explore alternative configurations that can eventually alleviate the structural deficiency of the ideal ABH structures, while maintaining similar ability for wave manipulation. In this study, the so-called imperfect two-dimensional ABH indentation with different tailored power-law-profiled is proposed and investigated. It is shown that the new indentation profile also enables a drastic increase in the energy density around the tapered area. However, the energy focalization phenomena and the process are shown to be different from those of conventional ABH structure. With the new indentation profile, the stringent power-law thickness variation in ideal ABH structures can be relaxed, resulting in energy focalization similar to a lens. Different from an ideal ABH structure, the energy focalization point is offset from, and downstream of indentation center, depending on the structural geometry. Additional insight on energy focalization in the indentation is quantitatively analyzed by numerical simulations using structural power flow. Finally, the phenomenon of flexural wave focalization is verified by experiments using laser ultrasonic scanning technique. [DOI: 10.1115/1.4034080]

Keywords: acoustic black hole, flexural wave focalization, finite element, laser ultrasonic technique

1 Introduction

Acoustic black hole phenomenon in a thin-walled structure was revealed by relatively recent research, which provides unique opportunities for structure-borne wave manipulation for a wide range of engineering applications. ABH effect originates from the propagation properties of the structure-borne waves in thin-walled structures. By shaping the wall thickness to a power-law profile (for one-dimensional beams, the local thickness $h(x)$ and the distance x from the tapered edge needs to satisfy $h(x) = \varepsilon x^m, (m \geq 2)$), the local phase (and the group) velocity of the flexural waves reduces gradually and approaches zero theoretically when reaching the zero-thickness end of the tapered wedge. In an ideal scenario, it results in zero reflection and total energy absorption with a small amount of damping materials [1–3] coated over the surface of the structure. For a plate, its thickness can also be tailored (to power-law-profiled indentations or pits), which allows trapping the structure-borne energy within the indentation area. ABH feature can be embedded in structures. Once achieved, it leaves room for structure-borne wave manipulation, the benefit of which is obvious for many engineering applications such as damped embedded ABHs effectively reduced the mechanical vibration and radiated sound power in a wide range of frequency [4], and the broadband characteristic

provides an effective approach to solve the limitations of current passive vibration control [5]. The strong concentration of vibration energy can facilitate more effective damping treatment for vibration control. In terms of energy utilization, it also provides new options for energy harvesting and enhances the harvesting efficiency.

However, an ideal ABH structure is difficult to be realized and to be used in practice. The former is due to the machining capability available and the unavoidable alteration to ABH structures imposed by particular ABH applications, while the latter being related to the structural deficiency resulting from the stringent thickness requirement of the ideal ABH profile. For example, truncations always exist in manufactured wedges due to the fact that minimum structural thickness that can be achieved depends on the limitations of the machining process. To address the issue, Bayod investigated the effect of a wedge extended at the sharp edge to form a thin plate of constant thickness, which was made specifically to overcome the difficulties associated with fabrication of very sharp wedges [6]. Two beams with ABH terminations, with thicknesses variation described as $h(x) = h_0(x + l_t)^m / l_t^m$ and $h(x) = h_t + (x + l_{ABH})^m(h_0 - h_t)/l_{ABH}^m$, were designed and tested [7]. Results showed that ABH effect will be adversely affected by geometrical and manufacturing imperfections. The reflection coefficient of a steel structure with a small truncated edge can be as large as 50–70% for one-dimensional ABH structure [8]. Typical two-dimensional ABH structures investigated in the literature usually contain a hole or a circular plate of constant thickness located at the center of the indentation area, with the latter being referred to as plateau hereafter. Inevitably, this can also

---

[1]Corresponding author.

affect the formation of the ideal ABH phenomenon. Experimentally measured frequency response functions of a two-dimensional ABH, with no or very small central hole, were reported [9]. Plates were designed based on a gradient index lens for guiding flexural waves to a particular region, which can be achieved by smoothly varying the thickness of the plate [10,11]. The results showed that the structural geometry (the termination, the plateau, and the thickness profile) has influence on energy concentration phenomenon. In an even broader sense, the additional structural components required for vibration control or energy-harvesting applications can also affect the ideal ABH structure. The use of damping materials, for example, can alter the ideal thickness profile of the ABH structure. Same applies when energy-harvesting elements such as piezoelectric patches or local oscillators are required [12]. All these result in nonideal performance as "black holes." It is relevant to mention that, from the point-of-view of engineering application, an ideal ABH structure is vulnerable in its load-carrying ability due to the extreme thin thickness in the tapered indentation area. Therefore, there is a need to explore other types of nonideal ABH structures, which have better structural properties while allowing effective energy focalization at the same time.

This paper attempts to tackle these issues by proposing a so-called imperfect two-dimensional ABH plate with a power-law-profiled indentation which may facilitate the realization of the flexural wave focalization feature, on the one hand, and overcome the structural problems of the ideal ABH structures, on the other hand. It differs from the conventional designs, in which the new configuration relaxes the strict thickness profile requirement of the existing design, which is difficult to achieve with unavoidable truncations at the tip of the tapered wedge. It provides a more general section profile of the indentation so that more geometric parameters can be tuned to achieve effective energy focalization and facilitate practical applications. As reported and well acknowledged in the literature, acoustic black whole effect can be achieved through two different stages: energy focalization and energy dissipation. While the former is mainly due to the changes of the thickness profile for slowing down the flexural wave speed, the latter can be achieved by using viscoelastic material layers over the tapered region, which is rather straightforward. Therefore, we only focus on the critical issue of the energy focalization with the use of the proposed imperfect ABH indentation in this paper. Underlying physics are explored through finite element method (FEM) simulations with influencing parameters being determined. Vibrational power flow concept or structural intensity is used to demonstrate the vibration energy transfer process, which allows tracking the propagation path in thin plates for flexural waves [13–15]. An experimental system is established by using a fixed-point acoustic emission (AE) sensor to collect the waves which are generated by a movable pulse laser. This method provides a series of snapshots to display the wave propagation process from the excitation point to the inspection region [16]. Based on the measurement, the energy focalization process in time-domain can be observed on the proposed plate with imperfect ABH indentation.

2 Bending Waves in Plate With Tailored Power-Law-Profiled Indentation

2.1 Governing Equation of Bending Waves.
The equation of motion describing flexural waves in a thin plate is written as [17]

$$\nabla^2(D\nabla^2 w) - (1-v)\left(\frac{\partial^2 D}{\partial x^2}\frac{\partial^2 w}{\partial y^2} - 2\frac{\partial^2 D}{\partial x \partial y}\frac{\partial^2 w}{\partial x \partial y} + \frac{\partial^2 D}{\partial y^2}\frac{\partial^2 w}{\partial x^2}\right)$$
$$+ \rho h \frac{\partial^2 w}{\partial t^2} = 0 \qquad (1)$$

where w is the transverse displacement of the plate; $D = Eh^3/12(1-v^2)$ is the flexural rigidity; E is the Young's modulus; v is the Poisson's ratio; ρ is the density; h is the thickness of the

plate; and t is the time variable. Assume that the thickness changes as $h = h(r)$. By neglecting the rotary inertia and the shear effects, the flexural wavenumber $k = \sqrt{k_x^2 + k_y^2}$, where k_x and k_y are, respectively, the wavenumbers in the x and y directions, can be written as [12]

$$k = (12k_l^2/h^2(r))^{1/4} \qquad (2)$$

where $k_l = \sqrt{\rho(1-v^2)\omega/E}$ is the longitudinal wavenumber in a thin plate with uniform thickness. Since $c = \omega/k$, the phase velocity can be expressed as

$$c = \sqrt{\omega h}\left[\frac{E}{12\rho(1-v^2)}\right]^{1/4} \qquad (3)$$

For a homogeneous isotropic flat plate of constant thickness, the phase velocity is proportional to the square root of the frequency. While for a plate with varying thicknesses, it also depends on its local thickness. The thickness-dependent feature of the phase velocity makes it possible to modulate wave propagation by means of local variation of the plate's thickness, which will be detailed in Sec. 2.2.

2.2 Tailored Power-Law Profile.
A schematic of the proposed rectangular plate with a two-dimensional pit of power-law-profile is presented in Figs. 1(a) and 1(b). The plate consists of a uniform portion of constant thickness h_2 from r_2 to the edge of the plate, a tapered region (from r_1 to r_2), and a plateau in the middle of the plate (from 0 to r_1) with a constant thickness h_1. The thickness of the tapered region gradually changes as

$$h(r) = \begin{cases} h_1, & (r \leq r_1) \\ a(r-r_1)^m + h_1, & (r_1 \leq r \leq r_2) \end{cases} \qquad (4)$$

The extreme case with $h_1 = r_1 = 0$ and $m \geq 2$ corresponds to an ideal ABH structure. By varying m, r_1, and h_1, various nonideal ABH profiles can be obtained.

For the proposed plate with variable thickness, the phase velocity in the inhomogeneous area ($r_1 \leq r \leq r_2$) can be expressed as (in polar coordinates)
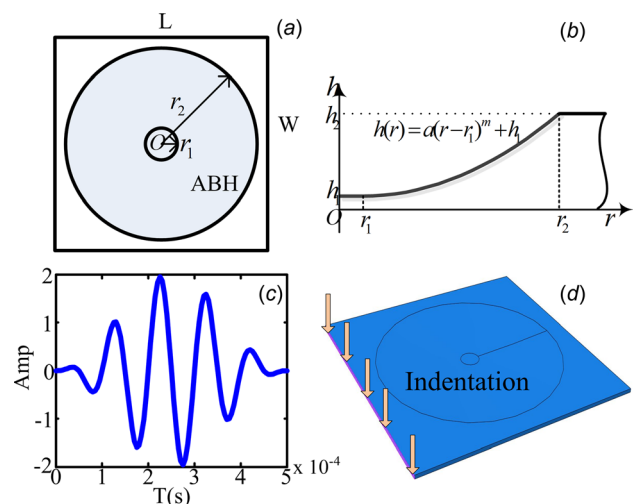

Fig. 1 Plate with a nonideally profiled ABH indentation ((a) and (b)), amplitude of five-period Hanning-windowed tone burst force (c), and normal drive position indicated (d)

$$c(r) = \left[\frac{E\omega^2 h^2(r)}{12\rho(1-v^2)} \right]^{1/4} \tag{5}$$

Therefore, the gradient index of the flexural wave velocity can be obtained by smoothly modifying the local thickness of the plate to trap waves within a given region. The refractive index of the material in optics is defined as $n = c_v/c_m$, where c_v and c_m correspond to the wave speed in vacuum and the material, respectively. Optical black hole can be obtained when graded refractive index is formed along a specific direction [18,19]. Expanding this definition to flexural wave in the present structure and assuming that all other elastic properties of the plate remain the same throughout the whole structure, the refractive index profile $n(r)$ in the inhomogeneous area of the plate can be expressed as a function of its thickness as

$$n(r) = \frac{c_0}{c(r)} = \sqrt{\frac{h_2}{a(r-r_1)^m + h_1}} \tag{6}$$

where c_0 is the wave speed in the uniform portion of the plate. Equation (6) describes the way in which the refractive index increases with decreasing thickness. It is important to note that, despite being an intrinsically dispersive medium, the refractive index does not depend on the frequency of the wave, but is related to the geometric parameters of the proposed structure. The refractive index gradient in the inhomogeneous area is expressed as

$$\frac{dn(r)}{dr} = -\frac{amh_2^{1/2}(r-r_1)^{m-1}}{2\left[a(r-r_1)^m + h_1\right]^{3/2}} \tag{7}$$

For a given initial incident flexural wave ray, relative deflection angles to propagation directions in the inhomogeneous area increase with the absolute value of the refractive index gradient. We mainly focus on the possible flexural wave focalization performance produced by such a two-dimensional nonideal ABH structure. Thus, the underlying physics about the dependence of the energy focalization on various structural parameters will be investigated in Sec. 4.

3 Numerical Analysis of Bending Waves in Platelike Structures With a Tailored Power-Law Profile

3.1 Numerical Model. In order to study the behavior of the propagating waves when interacting with the ABH region, a three-dimensional tapered plate model (480 mm × 480 mm × 5.86 mm) with a single power-law-profiled indentation of radius $r_1 = 0.02$ m was established. FEM simulations are carried out to help understand the basic principle of the energy focalization process and analyze the influence of parameter variations on the energy focal positions of the bending waves. The FE model was assembled and solved using ABAQUS. The indentation profile is obtained by revolving the cross profile about normal direction of the plate as shown in Fig. 1(b). The plate was simulated using C3D8 elements under plane stress conditions. At least ten elements per local wavelength were used to guarantee the calculation accuracy. Material and geometrical parameters used in the FE model are tabulated in Table 1.

Possible flexural wave focalization is first investigated under transient conditions. The structure with power-law-profiled

Table 1 Geometrical and material properties of the plate

Parameters	E	ρ	v	h_2	L	W	r_2
Value	72 GPa	2700 kg/m³	0.3	0.00586 m	0.48 m	0.48 m	0.2 m

indentation is excited by a unit Hanning-windowed tone burst force with a center frequency f as shown in Fig. 1(c). Since the fundamental mechanisms of the energy trapping remain the same for both ideal profile and the present indentation case, the use of the imperfect thickness profile will not change the broadband nature of the ABH structures which has been proved mathematically and numerically. The low cutoff frequency is related to the characteristic size of the ABH, which can be expressed as $[f \cdot D_{\mathrm{ABH}}/c_0] > 1$, in which D_{ABH} is the diameter of imperfect ABH indentation. For high-frequency waves, the phenomenon persists as long as the flexural elastic wave theory holds. The right-hand side edge of the plate is fixed, and the excitation source is applied along the left edge as shown in Fig. 1(d). Two representative cases ($f = 5$ kHz and $f = 10$ kHz) are examined to show that the location of the focal point is independent of the frequency.

3.2 Vibration Power Flow Analysis. As a way to describe the energy transport, vibratory power flow is investigated, defined as the rate of energy transmitted through a cross section of unit area in a structure. The time-averaged net power flow is given by

$$P(t) = \lim_{T \to \infty} \frac{1}{T} \int_0^T F(t)v(t)dt \tag{8}$$

where $F(t)$ and $v(t)$ are the instantaneous values of force and the corresponding velocity at a point, and t and T are the time and observation period. The time-averaged vibration power in the frequency domain is obtained by the Fourier transformation as

$$P(f) = \overline{F}(f)\overline{v}(f)^* \tag{9}$$

where $\overline{F}(f)$ and $\overline{v}(f)$ are the Fourier transformation of the domain signals $F(t)$ and $v(t)$, and the asterisk denotes complex conjugate. $P(f)$, called complex power, has two components: active power and reactive power. The active power is generally the quantity of interest since it is associated with the energy flow. The complex power $P(f)$ can be estimated by the one-sided cross-spectral density function $G_{vF}(f)$ of the signals, and the active power $P_a(f)$ is given by the real part of the complex power

$$P_a(f) = \mathrm{Re}\{G_{vF}(f)\} \tag{10}$$

The imaginary part of the complex power is the reactive power. Far-field power concept in isotropic plates has been established, which simplifies power flow estimation. The spacing is selected with regard to bending wavelength, such that the ratio of spacing to bending wavelength is 0.2 for upper frequency limit [18,19]. The use of this spacing criterion provides an optimal tradeoff between the reduced finite difference errors afforded by small sensor spacing. Using the "two-transducer" method [20–23], the active power also called as time-averaged power or intensity could be obtained as

$$I_x = \frac{2\sqrt{Dm'}}{d'} \mathrm{Im}\{G_{12}\} \tag{11}$$

where I_x is the active power in the direction of the transducer pair from 1 to 2 which are the two points along the x direction, G_{12} is the cross-spectrum of velocity signals, d' is the spacing, D is the flexural rigidity of the plate, m' is the mass per unit area of the plate, and Im is the imaginary part. Equation (11) is applicable both in the x- and y-directions of the plate.

4 Results and Discussion

4.1 Energy Distribution. For the purpose of investigating the energy focusing performance of the proposed structure, simulations were conducted and compared with its counterpart with a uniform thickness. Normal displacement fields at $f = 10$ kHz are

shown in Figs. 2(a) and 2(b) for both cases, respectively. Case (a) corresponds to the plate of uniform thickness, and case (b) corresponds to the plate with a tapered thickness, following $h(r) = a(r - r_1)^m + h_1$, where $m = 2, r_1 = 0.02 \, \text{m}$, and $h_1 = 0.001 \, \text{m}$. As shown in Fig. 2, the plane flexural waves propagate away from the source in the plate with uniform thickness before being bended near the ABH region. Compared with the ideal ABH structure, similar but different energy focalization phenomena are observed here. In the conventional ideal two-dimensional ABH case, all the rays of flexural waves are channeled toward the center of the indentation [24]. The imperfect ABH indentation and the conventional one were compared with the simulated displacement being shown in Fig. 3. Wave focuses within the center plateau in the conventional ABH case, while with nonzero h_1 and r_1, incident waves enter into the indentation area, detouring around the plateau and focusing to a confined region slightly downstream of the center plateau. Figures 2 and 3 also show that the wavelength of flexural waves is compressed, and a high energy density area is generated in the focalization area.

To further explain these observations and to visualize the results, it is helpful to plot the sum of squared displacement, which is defined as wave energy, over all the nodes within duration T as

$$E_i(x,y) = \int_0^T w_i^2(x,y,t)dt \qquad (12)$$

Figure 4 shows the simulated wave energy distribution within 1.3τ for the plates with variable thickness ($m = 2$,

$r_1 = 0.02 \, \text{m}$, and $h_1 = 0.001 \, \text{m}$) at frequencies $f = 10$ kHz and $f = 5$ kHz, respectively; and τ is the time for one-way flexural wave propagation from left to the right boundary in the uniform portion. Energy distribution is plotted, and the location is calculated within 1.3τ ($T_{f=10\,\text{kHz}} = 0.8$ ms and $T_{f=5\,\text{kHz}} = 1.2$ ms). The time at 1.3τ is chosen because the locations of focal point are found to remain the same within a period of time, about $1.1\tau - 1.3\tau$, after wave energy starts to gather. Meanwhile, the location of the focalization is not affected by reflection from the boundary within this time. It is observed from these images that the power-law-profiled indentation allows a substantial increase of vibrational amplitude when flexural waves travel through the ABH region, which results in obvious energy concentration. Apart from this, the overall trends in terms of displacement field are similar for both frequencies, and the location of the focal point is also roughly the same, independent of the frequency.

4.2 Indentations of Tailored Power-Law-Profile. To explain the aforementioned observations, additional simulations were carried out to investigate the effect of the geometric parameters, such as m, h_1, r_1, and that of the frequency on the energy focalization. The results of the energy distribution on the plate for $m = 2, r_1 = 0.02 \, \text{m}$, and $h_1 = 0.001 \, \text{m}$ are shown in Fig. 5. Note that a certain distance exists between the focal point of the incident wave and the center of the pit of the tapered plate. The focal positions are calculated as the peak of envelopes of the energy distribution. Figure 6 shows the relative index energy distribution at different cross sections perpendicular to the wave vector at 1.1τ and 1.3τ, which is normalized as energy ratio $\overline{E}_i(x,y) = E_i(x,y) / \max(E_i^0(x,y))$, where $E_i^0(x,y)$ is the energy distribution in the
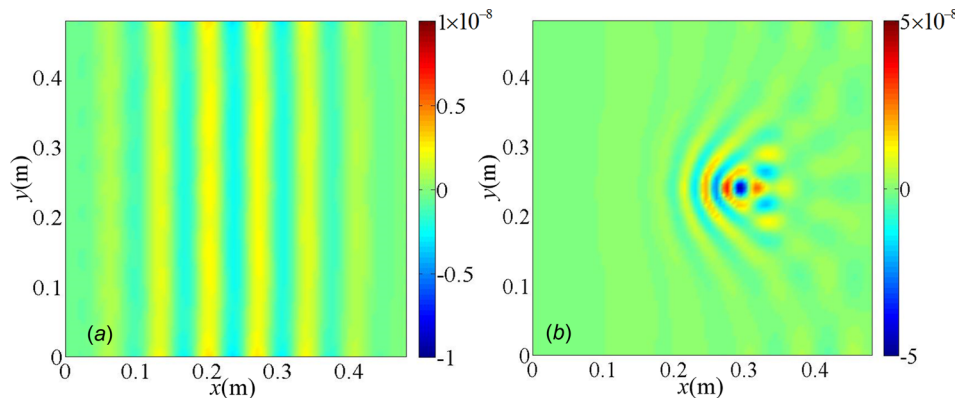

Fig. 2 Displacement at 10 kHz of plates: (a) with a uniform thickness and (b) with a variable thickness
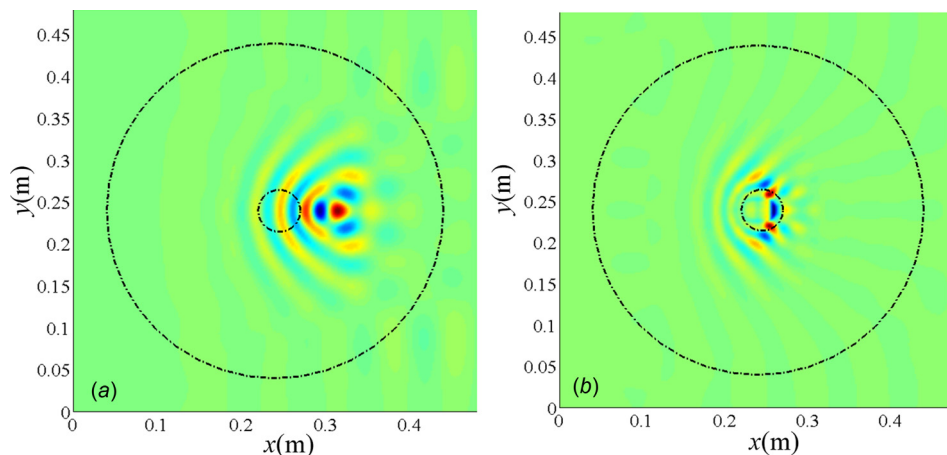

Fig. 3 Displacement at 10 kHz of plates: (a) the imperfect ABH ($h = \varepsilon(r - r_1)^m + h_1, m = 2$) and (b) the conventional ABH ($h = \varepsilon r^m, m = 2$)
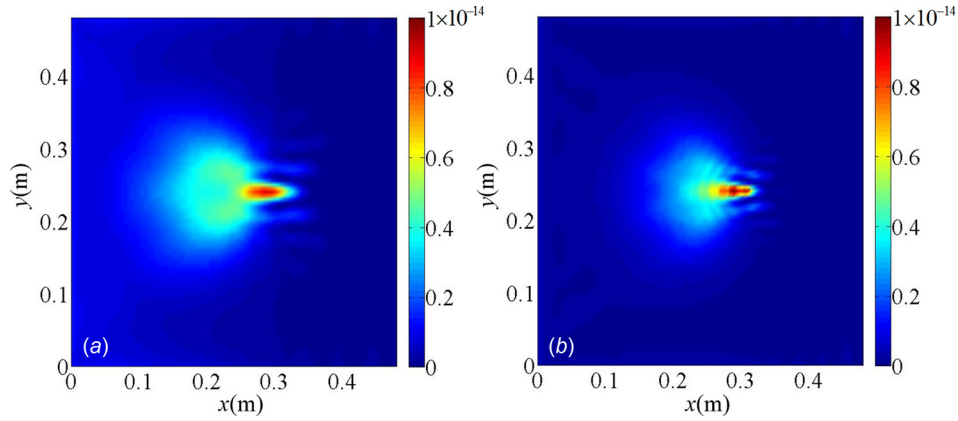
Fig. 4 Sum of squared displacement at $f = 5\,\text{kHz}$ (*a*) and $f = 10\,\text{kHz}$ (*b*) for plates with $m = 2, r_1 = 0.02\,\text{m}$, and $h_1 = 0.001\,\text{m}$
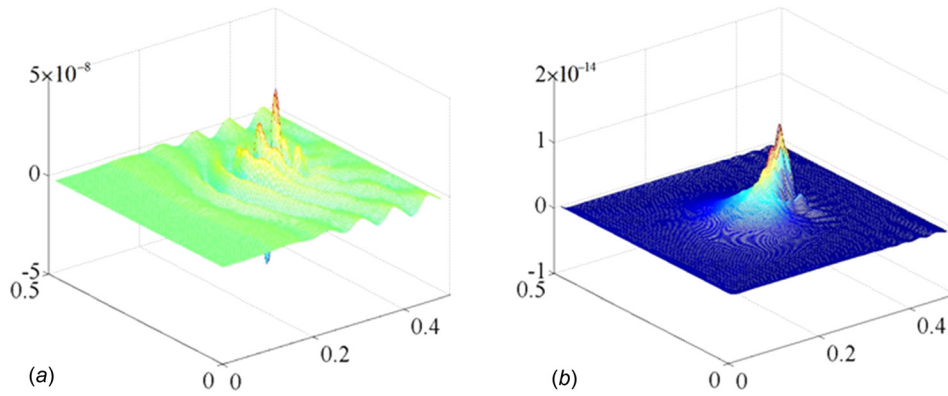

Fig. 5 Results of the energy distribution on the plate for (*a*) the displacement response and (*b*) the energy distribution
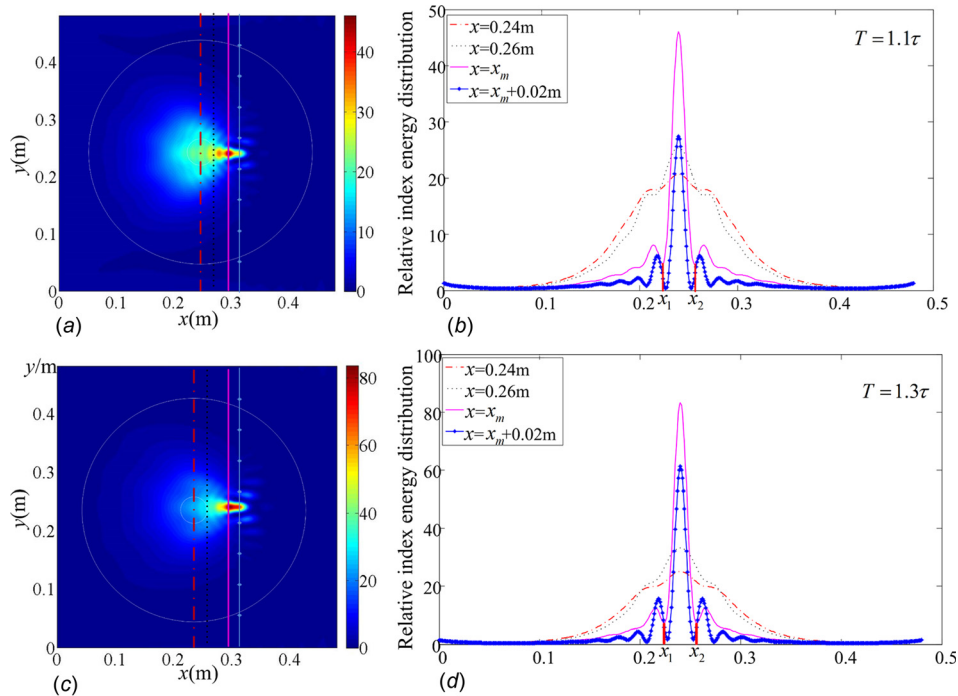

Fig. 6 Energy distribution at different cross sections and spots: (*a*) and (*b*) at $T = 1.1\tau$ and (*c*) and (*d*) at $T = 1.3\tau$
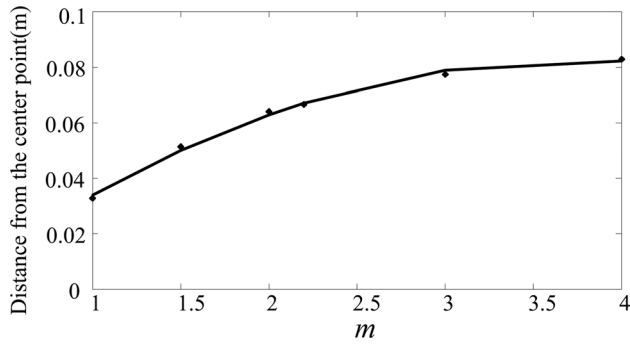
Fig. 7 The influence of the power-law function of thickness on the position of energy focalization for $r_1 = 0.02$ m and $h_1 = 0.001$ m

Fig. 10 The influence of the thickness of the central circular plateau on the position of energy focalization with $r_1 = 0.02$ m

Fig. 8 The refractive index gradient from r_2 to r_1 for $m = 2$, $m = 3$, and $m = 4$

Fig. 11 The refractive index gradient from r_2 to r_1 for $h_1 = 0.0005$ m, $h_1 = 0.001$ m, $h_1 = 0.0015$ m, and $h_1 = 0.002$ m

plate with uniform thickness. Four sections are chosen: section at $x = 0.24$ m; section at $x = 0.26$ m; section at the maximum value of the energy $(x = x_m)$, and section behind the maximum value of the energy $(x = x_m + 0.02$ m), respectively. The spot size is defined as the width of the highest peak which is $\Delta x = x_2 - x_1$ as shown in Fig. 6(b). In the present case, the spot size is 0.032 m, which is 6.7% of the width of plate.

The influence of the power index m in the thickness variation function on the focal position of energy focalization is shown in Fig. 7 for $r_1 = 0.02$ m and $h_1 = 0.001$ m. It can be seen that energy focalization always takes place downstream of the center point, further away from the center when m increases. Since flexural waves propagate through $r_2 = 0.2$ m than get to $r_1 = 0.02$ m, the refractive index gradient in the indentation from $r_2 = 0.2$ m to
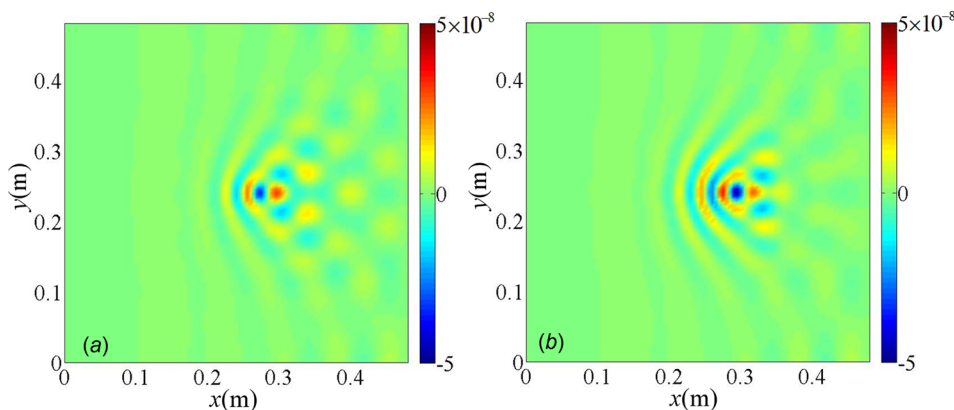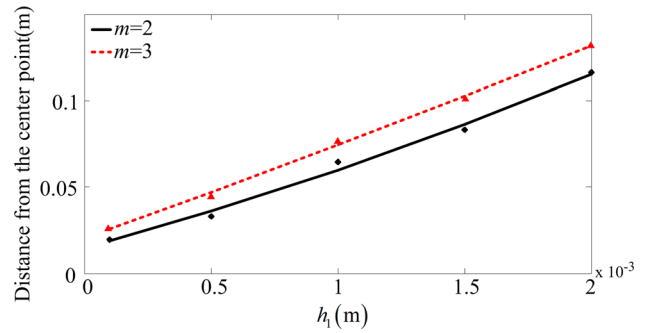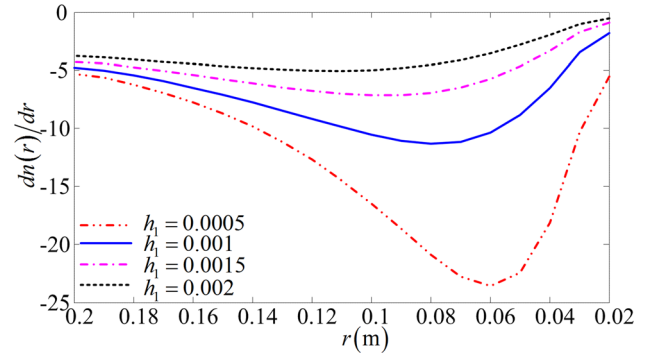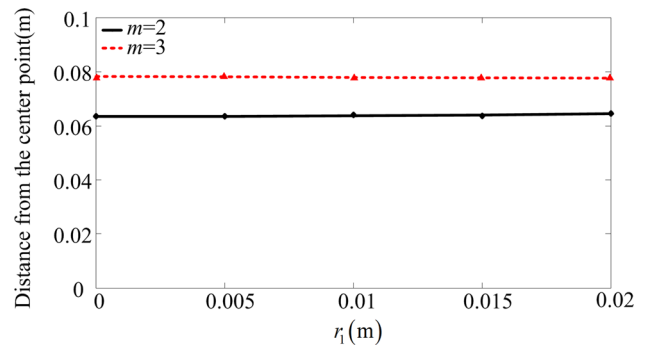

Fig. 12 The influence of the radius of circular plate on the focal position of energy focalization with $h_1 = 0.001$ m

Fig. 9 Simulated displacement of plates for $r_1 = 0.02$ m and $h_1 = 0.001$ m : (a) $m = 1$ and (b) $m = 1.5$
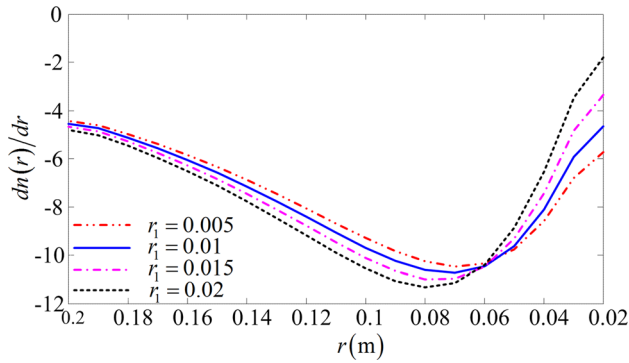
Fig. 13 The graded refractive index gradient for $r_1 = 0.005$ m, $r_1 = 0.01$ m, $r_1 = 0.015$ m, and $r_1 = 0.02$ m
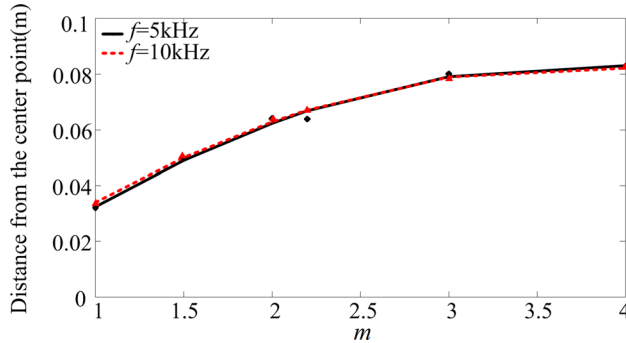

Fig. 14 Variation of focal position of energy focalization with the index m for different frequencies ($f = 5$ kHz and $f = 10$ kHz) with $r_1 = 0.02$ m and $h_1 = 0.001$ m

$r_1 = 0.02$ m is obtained as shown in Fig. 8. It can be seen that the refractive index gradient increases with m when the flexural wave first enters into the tapered area, however, it rapidly decreases when approaching the central plateau. Comparing $m = 4$ with $m = 2$, relative deflection angle for the given initial incident flexural wave rays is larger for 0.106 m $\leq r \leq 0.2$ m, but smaller for 0.02 m $\leq r \leq 0.106$ m, which makes the focalization further away from the center. Normal displacement fields for both $m = 1$ and $m = 1.5$ are shown in Fig. 9. It can be seen that energy focalization can still occur when m is smaller than two, similar to a lens.

Similar to the one-dimensional case, the minimum thickness of the structure (thickness of the central plateau) also has greater influence than the other structural parameters do on energy focalization. Figure 10 shows the influence of the thickness of the central circular plateau on the position of energy focalization for two m values with $r_1 = 0.02$ m. It is obvious that a larger h_1 creates larger offset of the energy focalization position during energy focalization process, outside the central circular plateau. As mentioned before, this thickness always exists in most practical situations to ensure minimum of structural strength. Besides, additional components such as damping layers or energy transducer can also increase the minimum thickness h_1. The refractive index gradient along the radius for different h_1 is shown in Fig. 11, which indicates that the smaller the thickness h_1, the larger the deflection angle for the same given initial incident flexural wave rays. In views of energy harvesting or noise and vibration control applications, future designs will need to emphasize the consideration of the influence of additional thickness. The influence of the radius of the circular plateau on energy focal position for different m values when $h_1 = 0.001$ m is illustrated in Fig. 12. It can be observed that the size of the plateau has negligible effect on the energy focalization position. Refractive index gradient for different r_1 is shown in Fig. 13, which shows little difference compared
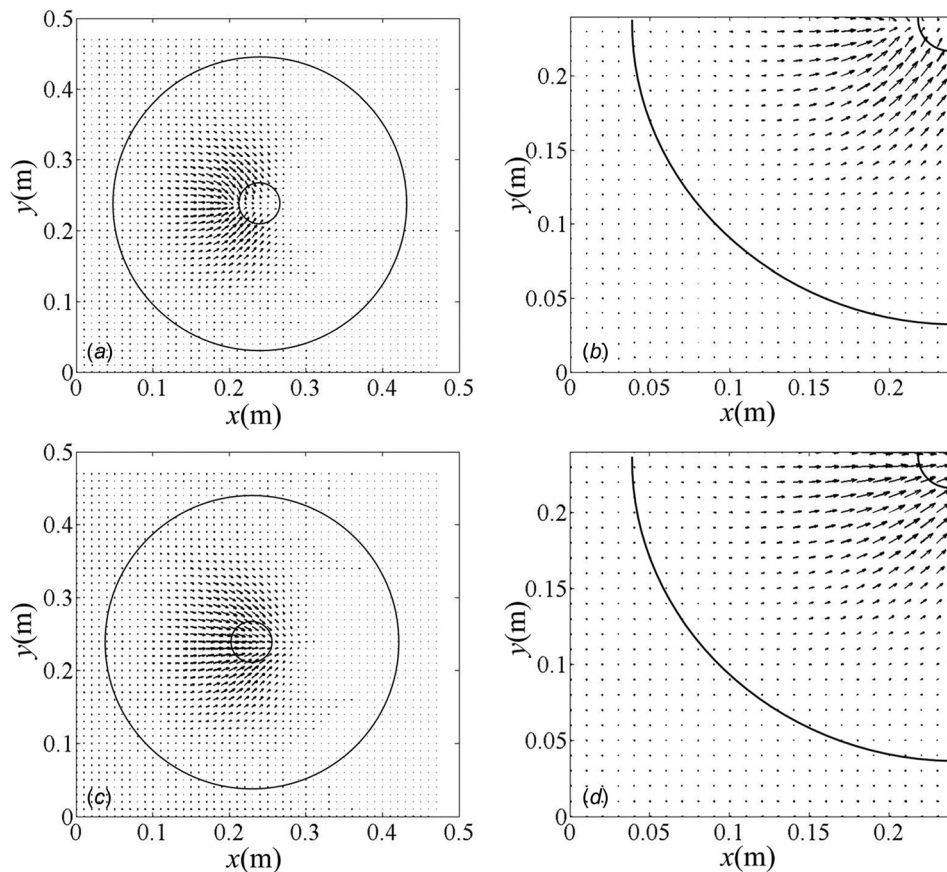

Fig. 15 Vector field of power flow in plate: (a) plate with $r_1 = 0.02$ m and $h_1 = 0.0005$ m, (c) plate with $r_1 = 0.02$ m and $h_1 = 0.001$ m, and (b) and (d) enlarged images for a quarter of (a) and (c)
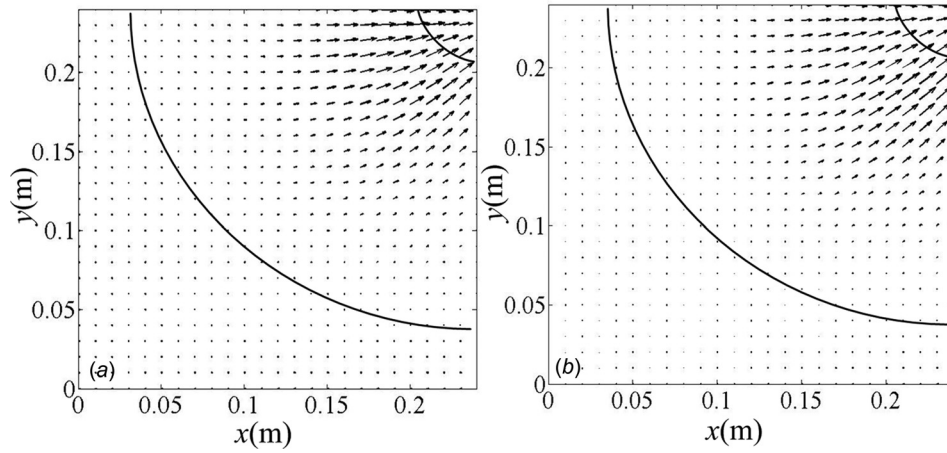
Fig. 16 Vector field of power flow in plate: (*a*) plate with $m = 2$, $r_1 = 0.02$ m, and $h_1 = 0.001$ m and (*b*) plate with $m = 3$, $r_1 = 0.02$ m, and $h_1 = 0.001$ m
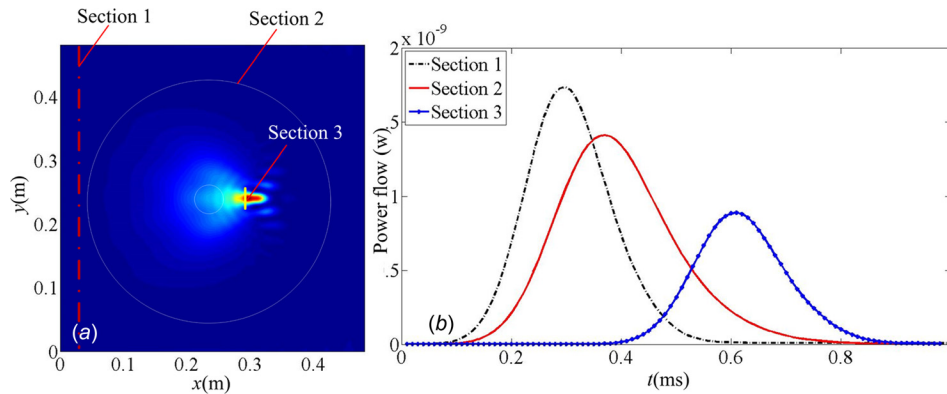

Fig. 17 Temporal change of power flow at different sections on the plate with $m = 2$, $r_1 = 0.02$ m, and $h_1 = 0.001$ m

with the influence of h_1 and m. It can be seen from Fig. 14 that the energy focalization points remain almost the same for $f = 5$ kHz and $f = 10$ kHz as observed previously. The calculation results also validate that the refractive index does not depend on the frequency of the wave, in agreement with Eq. (6).

4.3 The Transmission Path of Power Flow. The graphic representation of the power flow under the same excitation in Sec. 3.1 is plotted in Fig. 15 as a vector field. Two-dimensional interpolations based on the cubic interpolation algorithm are used to homogenize meshes and adjust the spacing which is used in two-transducer method. Figures 15(*a*) and 15(*c*) are the vector fields of the power flow in plate for $r_1 = 0.02$ m and $h_1 = 0.0005$ m and $r_1 = 0.02$ m and $h_1 = 0.001$ m, respectively. Figures 15(*b*) and 15(*d*) are the enlarged images for a quarter part of Figs. 15(*a*) and 15(*c*). Arrows denote the direction and magnitude of the vector field. It can be observed that the power flows are distinctly focused to a particular location of the plate. Comparison of Figs. 15(*b*) and 15(*d*) indicates that the path of wave propagation tends to the central part of the plate while h_1 decreases, confirming the observation in Figs. 10 and 11. Figure 16 shows the vector field with $m = 2$ and $m = 3$ for $r_1 = 0.02$ m and $h_1 = 0.001$ m. Comparison of the two cases shows that the relative deflection is larger in the inhomogeneous area near the plateau with a smaller m, which agrees well with the result in Figs. 7 and 8. Deflection of

energy flow vector to the center point of the indention is increased with the refractive index gradient, which is apparently changed with the parameter variations.

Additional insight on energy focalization in the indentation is quantitatively investigated, as shown in Fig. 17. Three different cross sections are chosen to calculate the temporal changes of the power flow: uniform portion perpendicular to incident wave direction; along the indentation boundary; and at the focalization spot, respectively, which explain how the energy focalization is affected by the change of parameters such as the power index m. The temporal change of the power flow on the boundary of the imperfect ABH indentation is presented in Fig. 18. As shown in the result, the power flow of the flexural wave through the boundary of the indentation increases with m under the plane wave incidence. The relative power flow is defined as a ratio $\bar{p} = p_i/p_1$, where p_i is the power flow on the ith cross section, and p_1 is that on cross section 1. Most of the energy flux passes into the indentation since the indentation accounts for a large proportion of the plate. Figure 19 shows the temporal change of the power flow on the section of the spot. It can be seen that energy focalization occurs earlier when m decreases due to the higher wave velocity. Power flow on the section of the focalization spot decreases with m since the plate thickness around the spot becomes smaller when m increases, resulting in a high energy concentration around the spot. In the present case, 58.25% of the total energy propagates through the section of the spot which is 6.7% of the width of plate
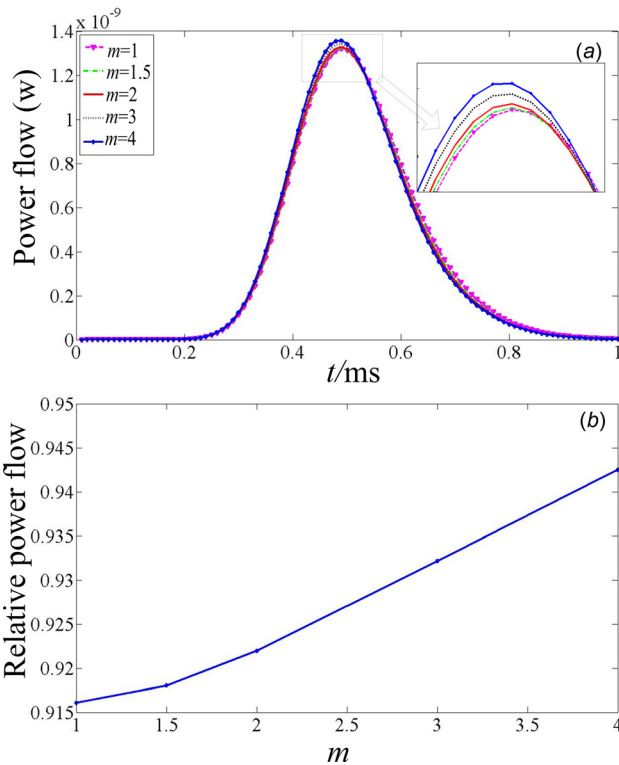
Fig. 18 The influence of index m on power flow with $r_1 = 0.02$ m and $h_1 = 0.001$ m : (a) temporal change of power flow at section 2 and (b) ratio of the power flow at section 2 to the power flow at section 1
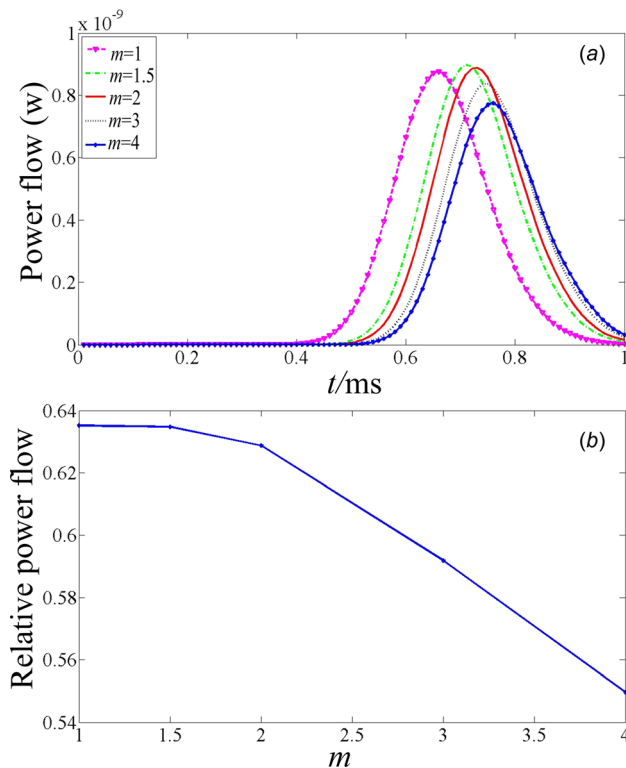

Fig. 19 The influence of index m on the power flow with $r_1 = 0.02$ m and $h_1 = 0.001$ m: (a) temporal change of power flow at section 3 and (b) ratio of the power flow at section 3 to the power flow at section 1

with $m = 2, r_1 = 0.02$ m, and $h_1 = 0.001$ m. This method provides the possibility to trace flexural wave propagation in time-domain conveniently.

5 Experimental Confirmation and Discussion

A laser ultrasonic scanning technique based experimental system is shown in Fig. 20. The system includes a laser generator (YAG laser, Ultra-100, Quantel Corp., Ogden, UT) for the generation of elastic waves, an AE sensor (M31, Fuji Ceramics Corp., Fujinomiya, Japan) for measurement, a pre-amplifier (A1002, Fuji Ceramics Corp., Fujinomiya, Japan), an AE analyzer (AE9922, NF Corp., Fujinomiya, Japan), a high-speed digitizer (PXI-5105, NI Corp., Austin, TX) to sample signals, and an analog output module (cRIO-9263, NI Corp., Austin, TX) to control a two-dimensional laser mirror scanner (TSH8203H, Century Sunny Corp., Beijing, China). The laser generator produces a pulse laser with a repeating frequency of 20 Hz, which is used to generate elastic waves when irradiated on the structure. In the measurement, the AE sensor is fixed on the structure, but the excitation point is scanned over the inspection region of the structure with a given two-dimensional resolution by rotating the two-dimensional mirror. The response of the AE sensor to laser excitation at different scanning points is sampled and recorded [16,25,26]. Based on the reciprocal theorem in elastodynamics, the obtained signals in three dimensions, one time dimension and two spatial dimensions, can be used to reconstruct the dynamic acoustic wave field in the inspection region. For a given time instant, the wave field at a specific moment can be displayed.

As shown in Fig. 21, the tested steel plate has a dimension $L \times W \times H = 350$ mm $\times 240$ mm $\times 5$ mm. The thickness of indentation profile follows $h(r) = 7.5 \times 10^{-4} \times (r - 20)^2 + 0.2, (20 \leq r \leq 100)$ (in mm), the central point O of indentation is 130 mm away from the right edge on symmetry axis, and the thickness of a plateau in the middle of the plate is 0.2 mm. The steel plate is used mainly for the ease of machining the ABH, which allowed avoiding the distortion problem when using aluminum. Moreover, the velocity ratios $(v_{al}/v_{steel} = 0.94)$ of the steel and aluminum are actually very close, which involve basically very similar physical phenomena. The indentation first went through a milling process with a positive allowance of 0.3–0.4 mm. After tempering and aging treatment, machining operation finishes with a positive allowance of 0.05 mm to prevent cracking by wire-electrode cutting. The thickness of the steel plate used in the experiment was measured, giving a maximum error of 0.073 mm at $r = 50$ mm. The AE sensor is placed on the same side of indentation with a distance d away from the center point of power-law-profiled indentation. The flat side of the plate is scanned by the movable laser point, and the inspection region is $L_i \times W_i = 270$ mm $\times 220$ mm with a distance $\Delta = 10$ mm to the edge. The spatial scanning interval is 1 mm giving a total of 59,891 scanning points. The signal is filtered with the band-pass frequency from 15 kHz to 25 kHz. To obtain the waves field in the inspection region, the sampling frequency was set to be 1×10^7/s and the duration of data acquisition was set to 250 μs (2500 sampling point) for each excitation to ensure that the flexural waves generated by laser at the right edge of inspection region ($x = 270$ mm) can arrive at the AE sensor in the duration.

The wavefields from both experimental test and numerical simulations for $d = 150$ mm are shown in Fig. 22. It can be seen that waves propagate from the source to the inspection region and then focus to a confined region slightly downstream of the central point. Circular wavefronts are formed from the signal of AE sensor, as flexural wave rays that propagate through the indentation are deflected due to the refractive index gradient. This is demonstrated in our analysis which governs the focalization process and mechanism. Focalization takes place for both the circular wavefronts and plane wavefronts with different incident angles. In the experimental measurements, the results are inevitably influenced by some unavoidable inaccuracies and uncertainties such as the
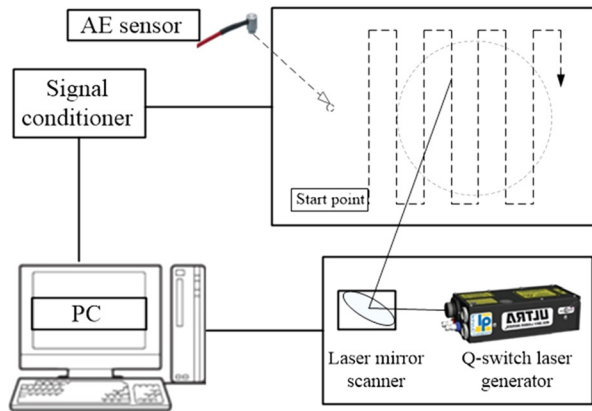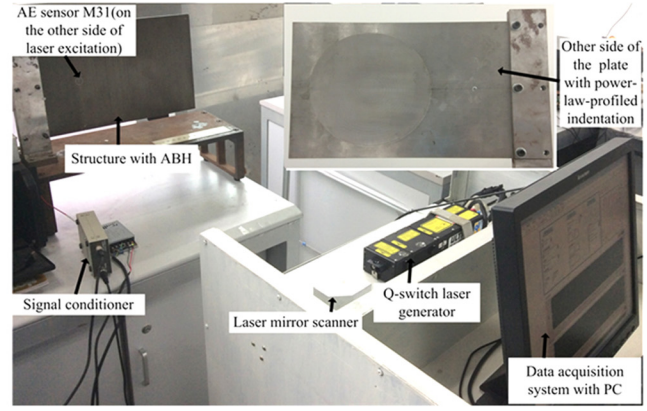
Fig. 20   Experimental system: (*a*) schematic diagram of the laser ultrasonic system and (*b*) experimental setup of the laser ultrasonic scanning system
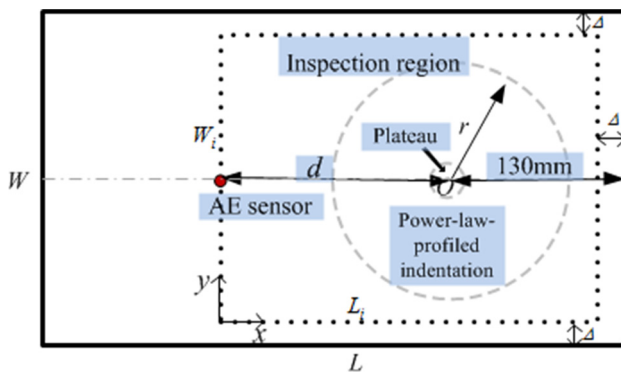

Fig. 21   Diagrammatic sketch of experimental plate

machining precision of the test sample and signal-to-noise ratio of the laser ultrasonic scanning system. Therefore, it is very challenging to get extremely accurate results. Nevertheless, we believe that the experimental results have clearly validated the phenomenon of flexural wave focalization in a qualitative manner. Snapshot of the wavefield in Figs. 22(*b*) and 22(*d*) shows noticeable circumferential nonuniformity of the wave, which is an interesting phenomenon to be further investigated. Wave energy is used again to evaluate the phenomenon of focalization as before. Assuming the response of AE sensor is $v(x, y, t)$, which is a signal closely related with $w(x, y, t)$, wave energy distribution is calculated by $E_i(x, y) = \int_0^T v^2(x, y, t)dt$. Figure 23 shows the measured and simulated normalized wave energy distribution as $\overline{E}_i(x, y) = E_i(x, y)/\max(E_i(x, y))$, which verifies again the phenomenon of energy focalization.
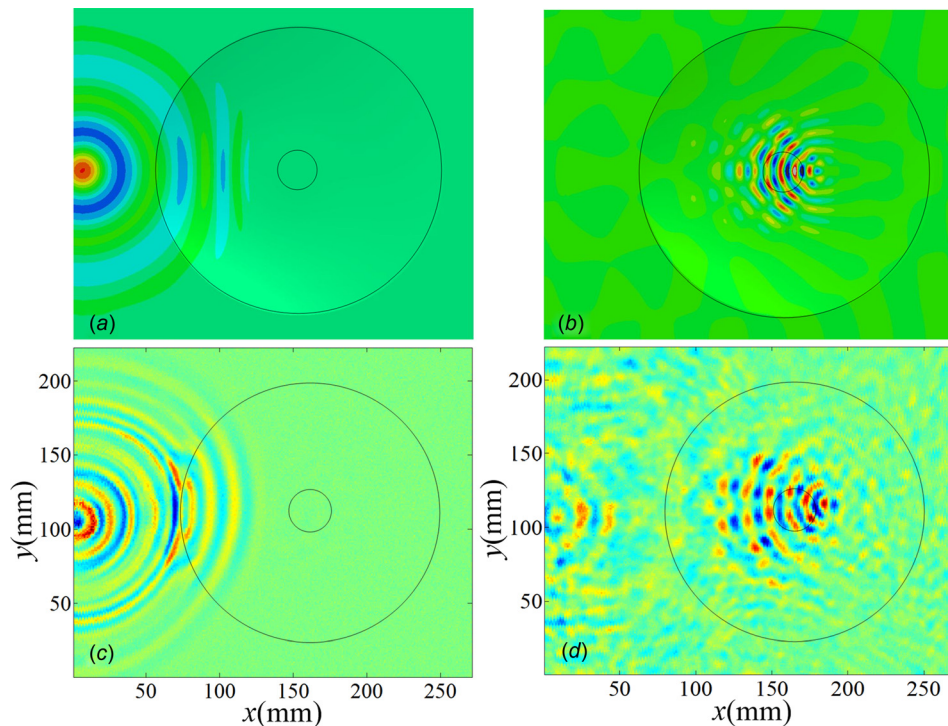

Fig. 22   The wavefields for *d* = 150 mm: (*a*) and (*b*) simulated wavefields at different times and (*c*) and (*d*) experimental wavefields at corresponding time
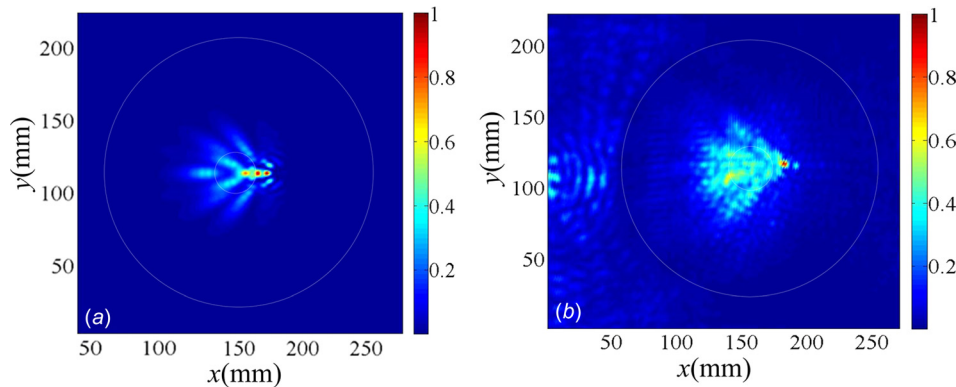
Fig. 23 The normalized wave energy distribution: (a) simulated result and (b) experimental result

6 Conclusions

In this paper, an ABH plate with a general power-law-profiled indentation is proposed and investigated. The proposed structure shows a more realistic thickness profile and produces similar but different energy focalization phenomena as the ideal ABH does. The new profile with a central plateau also ensures better structural strength as compared to the conventional ideal ABH structures. The new profile allows for a smooth reduction of the phase velocity of flexural waves and energy focalization in the vicinity, but downstream of the indentation center without, however, having to obey the stringent limitation imposed by the ideal ABH thickness profile (m no less than two).

Features of the new indentation profile have been studied through both numerical simulations and experiments in time-domain. The influence of the structural parameters on ABH effect and on the focalization positions of the bending wave has also been analyzed. The results indicate that the minimum thickness of the structure in the indentation pits (thickness of the central circular plateau) has a greater impact than the other parameters do, and the influence of the power index m on the energy focalization was also discussed. Meanwhile, the refractive index or energy focalization does not depend on the frequency of the wave. Numerical calculations on the structural power flow allow clear visualization of the energy transport and focalization of flexural wave in the vicinity of the indentation area, which are obviously under the influence of structural parameters.

It is relevant to note that, although the present work provides guidelines to choose various parameters defining the thickness profile of the indentation, smaller h_1 is definitely better for ABH indentation. However, engineering design should be a compromised solution among various considerations such as the structural strength and integrity of the entire structure. Further analyses should also be carried out targeting more specific issues for potential vibration control or energy-harvesting applications.

References

[1] Krylov, V. V., and Winward, R. E. T. B., 2007, "Experimental Investigation of the Acoustic Black Hole Effect for Flexural Waves in Tapered Plates," J. Sound Vib., **300**(1), pp. 43–49.

[2] Krylov, V. V., 2002, "Acoustic 'Black Holes' for Flexural Waves and Their Potential Applications," Institute of Acoustics Spring Conference, Salford, UK, pp. 25–27.

[3] Krylov, V. V., and Tilman, F. J. B. S., 2004, "Acoustic 'Black Holes' for Flexural Waves as Effective Vibration Dampers," J. Sound Vib., **274**(3), pp. 605–619.

[4] Feurtado, P. A., and Conlon, S. C., 2016, "Experimental Investigation of Acoustic Black Hole Dynamics at Low, Mid, and High Frequency," ASME J. Vib. Acoust. **138**(6), p. 061002.

[5] Zhao, L., 2016, "Passive Vibration Control Based on Embedded Acoustic Black Holes," ASME J. Vib. Acoust., **138**(4), p. 041002.

[6] Bayod, J. J., 2011, "Experimental Study of Vibration Damping in a Modified Elastic Wedge of Power-Law Profile," ASME J. Vib. Acoust., **133**(6), p. 0161003.

[7] Denis, V., Gautier, F., Pelat, A., and Poittevin, J., 2015, "Measurement and Modelling of the Reflection Coefficient of an Acoustic Black Hole Termination," J. Sound Vib., **349**, pp. 67–79.

[8] Krylov, V. V., 2004, "New Type of Vibration Dampers Utilising the Effect of Acoustic 'Black Holes'," Acta Acust. Acust., **90**(5), pp. 830–837.

[9] Bowyer, E. P., O'Boy, D. J., Krylov, V. V., and Gautier, F., 2013, "Experimental Investigation of Damping Flexural Vibrations in Plates Containing Tapered Indentations of Power-Law Profile," Appl. Acoust., **74**(4), pp. 553–560.

[10] Schiller, N. H., Lin, S. C. S., Cabell, R. H., and Huang, T. J., 2012, "Design of a Variable Thickness Plate to Focus Bending Waves," ASME Paper No. NCAD2012-1330.

[11] Climente, A., Torrent, D., and Sanchez-Dehesa, J., 2013, "Omnidirectional Broadband Insulating Device for Flexural Waves in Thin Plates," J. Appl. Phys., **114**(21), p. 214903.

[12] Zhao, L., Conlon, S. C., and Semperlotti, F., 2014, "Broadband Energy Harvesting Using Acoustic Black Hole Structural Tailoring," Smart Mater. Struct., **23**(6), pp. 182–186.

[13] Huh, Y. C., Chung, T. Y., Lee, J. W., and Kim, J. K., 2015, "Damage Identification in Plates Using Vibratory Power Estimated From Measured Accelerations," J. Sound Vib., **336**(336), pp. 106–131.

[14] Han, F., Bernhard, R. J., and Mongeau, L. G., 1997, "Energy Flow Analysis of Vibrating Beams and Plates for Discrete Random Excitations," J. Sound Vib., **208**(5), pp. 841–859.

[15] Mandal, N. K., Rahman, R. A., and Leong, M. S., 2003, "Structure-Borne Power Transmission in Thin Naturally Orthotropic Plates: General Case," J. Vib. Control, **9**(10), pp. 1189–1199.

[16] Zhang, C., Qiu, J., and Ji, H., 2014, "Laser Ultrasonic Imaging for Impact Damage Visualization in Composite Structure," EWSHM—7th European Workshop on Structural Health Monitoring. Laser Ultrasonic Imaging for Impact Damage Visualization in Composite Structure, La Cité, Nantes, France, July 8–11, pp. 2199–2205.

[17] Timoshenko, S., Young, D. H., and Weaver, W., 1974, *Vibration Problems in Engineering*, Wiley, New York.

[18] Qiu, J., Tan, J. Y., Liu, L. H., and Hsu, P. F., 2011, "Infrared Radiative Properties of Two-Dimensional Square Optical Black Holes," J. Quant. Spectrosc. Radiat. Transfer, **112**(16), pp. 2584–2591.

[19] Wang, H. W., and Chen, L. W., 2011, "A Cylindrical Optical Black Hole Using Graded Index Photonic Crystals," J. Appl. Phys., **109**(10), pp. 645–647.

[20] Noiseux, D. U., 1970, "Measurement of Power Flow in Uniform Beams and Plates," J. Acoust. Soc. Am., **47**(1B), pp. 238–247.

[21] Kay, K. Q., and Swanson, D. C., 1996, "Error in Bending Wave Power Measurements Resulting From Longitudinal Waves," Noise Control Eng. J., **44**(4), pp. 185–192.

[22] Mandal, N. K., Rahman, R. A., and Leong, M. S., 2005, "Experimental Investigation of Vibration Power Flow in Thin Technical Orthotropic Plates by the Method of Vibration Intensity," J. Sound Vib., **285**(3), pp. 669–695.

[23] Lee, H. P., Lim, S. P., and Khun, M. S., 2006, "Diversion of Energy Flow Near Crack Tips of a Vibrating Plate Using the Structural Intensity Technique," J. Sound Vib., **296**(3), pp. 602–622.

[24] Krylov, V. V., 2007, "Propagation of Plate Bending Waves in the Vicinity of One- and Two-Dimensional Acoustic Black Holes," First International ECCOMAS Thematic Conference on Computational Methods in Structural Dynamics and Earthquake Engineering, Rethymno, Greece, June 13–16.

[25] Zhang, C., Ji, H., Qiu, J., and Wu, Y., 2014, "Research on Interference Energy Calculation Method in Laser Ultrasonic Technique," Acta Opt. Sin., **34**(7), p. 714001.

[26] Wu, Y., Qiu, J., Zhang, C., Zhu, K., and Ji, H., 2014, "A Method to Improve the Visibility of the Damage-Reflected Wave," Chin. J. Lasers, **41**(3), p. 0308001.